SLAC-PUB-14845

CO Hydrogenation to methanol on Cu-Ni Catalysts: Theory and Experiment

Felix Studt,[a*] Frank Abild-Pedersen,[a] Qiongxiao Wu,[b] Anker D. Jensen,[b*] Burcin Temel,[c] Jan-Dierk Grunwaldt,[d] Jens K. Nørskov[a]

a SUNCAT Center for Interface Science and Catalysis, SLAC National Accelerator Laboratory, Menlo Park, CA, United States and Department of Chemical Engineering, Stanford University, Stanford, CA, United States
b Department of Chemical and Biochemical Engineering, Technical University of Denmark, Søltofts Plads, Building 229, 2800 Kgs. Lyngby, Denmark
c Haldor Topsøe A/S, Nymoellevej 55, 2800 Kgs. Lyngby, Denmark
d Institute of Chemical Technology and Polymer Chemistry, Karlsruhe Institute of Technology, Engesserstr. 20, 76131 Karlsruhe, Germany
*Corresponding author: studt@slac.stanford.edu

Abstract

We present density functional theory calculations for CO hydrogenation on different transition metal surfaces. Based on the calculations trends are established over the different monometallic surfaces and scaling relations of adsorbates and transition states that link their energies to only two descriptors, the carbon oxygen binding energies, are constructed. A microkinetic model of CO hydrogenation is developed and a volcano shaped relation based on the two descriptors is obtained for methanol synthesis. A large number of bimetallic alloys with respect to the two descriptors is screened and CuNi alloys of different surface composition are identified as potential candidates. These alloys, proposed by the theoretical predictions, are prepared using an incipient wetness impregnation method and tested in a high pressure fixed bed reactor at 100 bar and 250 to 300 °C. The activity based on surface area of the active material is comparable to that of the industrially used $Cu/ZnO/Al_2O_3$ catalyst. We employ a range of characterization tools such as inductively coupled plasma optical emission spectroscopy (ICP-OES) analysis, in-situ X-ray diffraction (XRD), and in-situ transmission electron microscope (TEM) to identify the structure of the catalysts.

Introduction

Methanol is among the top ten petrochemicals produced in the world, with its main applications being the production of formaldehyde, acetic acid, olefins and methyl-tertbutyl ether, a gasoline additive to boost the octane number.[1] Apart from its use as a base chemical, methanol has also been suggested as a transportation fuel in an alternative methanol-based economy.[2] A large number of different catalysts have been tested for methanol synthesis, and $Cu/ZnO/Al_2O_3$ catalysts have been established as the catalyst of choice in industry. These catalysts convert synthesis gas, a mixture of CO, CO_2 and H_2, at 230-280 °C and 50-120 bar with high selectivity into methanol.[3] Despite several decades of research there are still a number of open questions regarding the nature of the active site[4,5] and the reaction mechanism of $Cu/ZnO/Al_2O_3$ catalysts.[1] Deactivation of the catalyst poses one of the biggest

Work supported in part by US Department of Energy contract DE-AC02-76SF00515.

problems; more than one-third of the activity is lost after the first 1000h of operation, and this fact often determines the economic lifetime of the catalyst.[6,7] Apart from $Cu/ZnO/Al_2O_3$ numerous different catalysts with other promotors such as MnO_2,[8,9] ZrO_2,[10] Ga_2O_3,[11] and B_2O_3,[12] have been studied. Among the noble metals such as Pd, Pt and Ir, Pd stands out in particular with a high activity and selectivity for methanol formation,[13] although high selectivities towards methane have been reported for Pd catalysts as well. Potassium-promoted MoS_2 has a significant activity for methanol synthesis, although the selectivity is only about 50%.[14] For the above mentioned reasons, there are continuous interests in catalysts with improved properties.

Here we present extensive density functional theory calculations for the CO hydrogenation on a Cu(211) surface. After the identification of the lowest energy pathway, the study is extended to different transition metal surfaces. We establish scaling relations for adsorbates[15] as well as transition-states[16,17,18,19,20,21] and use them to reduce the number of independent variables that determine the overall activity to only two. A micro-kinetic model is developed and the theoretical turnover frequency is calculated as a function of the two descriptors resulting in an activity volcano for this reaction. Based on screening of a large number of bimetallic alloys, CuNi alloys, rich in Cu at steps, are suggested as active and selective methanol synthesis catalysts. The theoretically predicted catalysts have been prepared using an incipient wetness impregnation method and tested in a high pressure fixed bed reactor at 100 bar and 250 to 300 °C. The activity based on surface area of the active material has been shown to be comparable to that of the industrially used $Cu/ZnO/Al_2O_3$ catalyst. Inductively coupled plasma optical emission spectroscopy (ICP-OES) analysis, in-situ X-ray diffraction (XRD), and in-situ transmission electron microscopy (TEM) have been used to identify the structure of the catalysts. Preliminary studies of the stability of the Ni-Cu catalyst system have been performed, showing the catalyst to increase its activity with time on stream.

Results

There are several theoretical studies dealing with CO hydrogenation on Cu surfaces in the literature. However, most of these studies employ the (111)[22] or (100)[23] facets of Cu, or deal with small Cu clusters.[24] We chose the 211 surface for the parent study since it is known that the active site of the industrially used $Cu/ZnO/Al_2O_3$ catalyst has defects such as stacking faults that can be modeled by stepped 211 surfaces.[4,25,26] It has also been shown that all intermediates during hydrogenation of CO to methanol bind stronger on the 211 facet of Cu when compared to Cu(100) and (111).[27]

Figure 1 shows the CO hydrogenation pathway over stepped Cu(211) as obtained from DFT calculations. CO hydrogenation occurs via hydrogenation of the carbon end of adsorbed CO; CO gets hydrogenated to HCO, H_2CO and finally to H_3CO. While CO and HCO bind to the surface through the carbon end, H_2CO lies flat and binds through both, its C and O atoms. Methoxy (H_3CO) flips around and binds through the

oxygen atom. Hydrogenation of methoxy is the last step in the reaction cascade to yield methanol. In contrast, hydrogenation of the oxygen end involving the intermediates COH, HCOH, and H_2COH is associated with much higher barriers and all intermediates are higher in energy than their carbon hydrogenated counterparts. As can be seen from the lowest energy pathway in Figure 1 (blue line), hydrogenation of CO and H_3CO have the highest barriers of 0.88 and 1.27 eV, respectively.

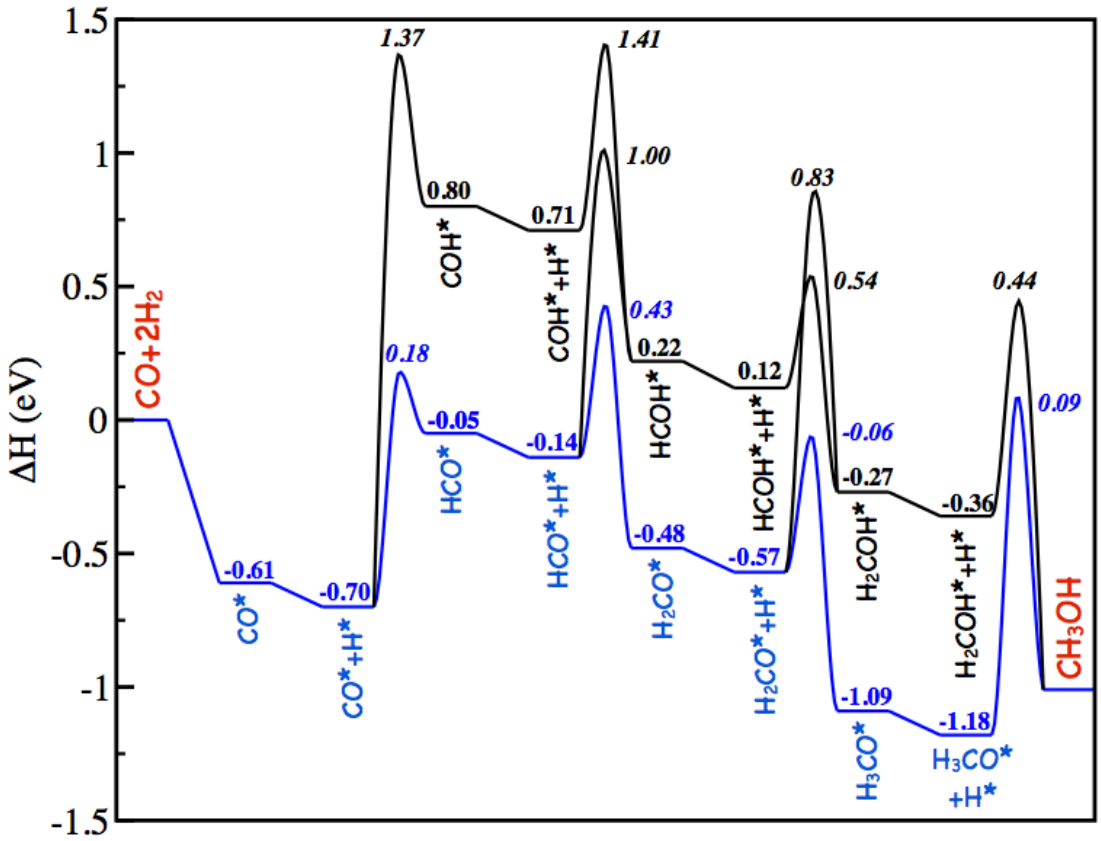

Figure 1. *The possible energy pathways for CO hydrogenation on the stepped Cu(211) surface. Intermediates marked with * are adsorbed on the surface. All energies are relative to CO and H_2 in the gas-phase. The lowest energy pathway is depicted in blue.*

Having identified the reaction path for the hydrogenation of CO on the copper surface, we will now extend the study to other transition-metal surfaces. This relies on establishing trends in adsorption and transition-state energies from one surface to another and also the assumption that the same pathways would be beneficial on the other surfaces. In order to obtain these trends, calculations of H, CO, HCO, H_2CO, and H_3CO adsorption as well as transition states of reactions CO+H->HCO, HCO+H->H_2CO, H_2CO+H->H_3CO, and H_3CO+H->CH_3OH have been performed for a number of transition metal surfaces including Ag, Au, Pd, Pt, Rh, Ni, and Ru.

We will now introduce the concept of scaling and use this concept to reduce the number of independent variables that would otherwise be necessary for a satisfactory description of trends in CO hydrogenation to methanol. We have previously shown that the adsorption energy of an adsorbate AH_x that binds

through atom A on a transition-metal surface will scale linearly with the adsorption energy, ΔE_A, of atom A.[15] The slope of this correlation is usually given by simple bond-counting arguments.[28] The intercept of the scaling line with the ΔE_A=0 axis can be obtained from a single calculation on one transition-metal surface. These scaling relations have been proven useful for the description of complex reaction networks by only few parameters[29,30,31,32] and there have already been successful attempts in the discovery of leads for new catalytic materials based on fast screening of these simple parameters.[33,34,35]

Figure 2 shows the scaling relations for intermediates CO, HCO, H_2CO, and H_3CO. Both, CO, and HCO are found to scale relatively well with the chemisorption energy of carbon (ΔE_C). H_2CO binds with both, the carbon and oxygen atom to the surfaces. Simple bond counting arguments for a broken double bond lead to a scaling with ¼ carbons and ½ of oxygens chemisorption energy (ΔE_O), while adsorption is thermoneutral for noble metals.[36] As can be seen from Figure 2, this assumption gives a fairly good scaling description of H_2CO. Finally, H_3CO, which binds through oxygen to the surface, is found to scale with approximately ½ ΔE_O. Hydrogen adsorption is modeled with ΔE_C as reported previously.[31]

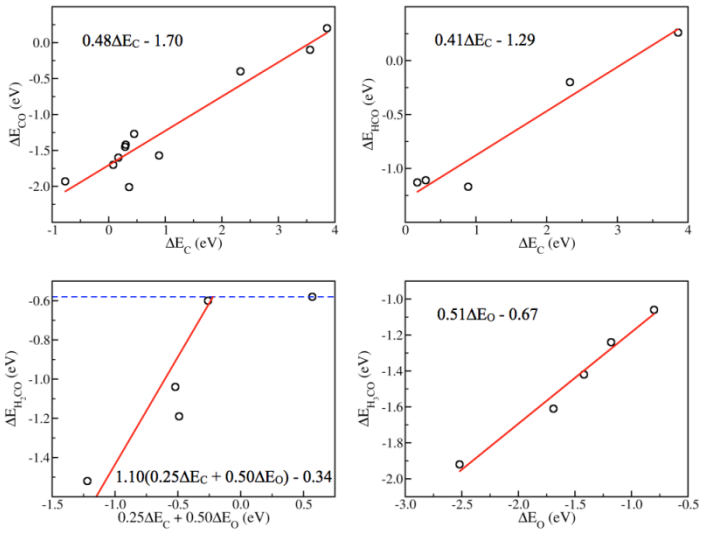

***Figure 2**. Scaling relations of adsorption energies of the 4 different intermediates of the lowest energy pathway from Figure 1. The adsorption energies are calculated on the stepped (211) surfaces of various transition metals and are taken relative to CO and H_2 in the gas-phase. Zero-point corrections are not included in the adsorption energies. Energies are plotted as a function of ΔE_C for CO, and HCO adsorption, ΔE_O in the case of H_3CO adsorption, and both ΔE_C and ΔE_O in the case of H_2CO adsorption. The red line is obtained by the best fit through data points; the slope and intercept of the fit is given in each figure. The blue line in the figure of H_2CO scaling represents the energy of H_2CO in the gas-phase relative to CO and H_2, a data point on the blue line corresponds to an H_2CO adsorption energy of zero.*

For estimating the rates we will use scaling relations for transition-state energies (Brønsted-Evans-Polanyi (BEP) relations) in a similar way. It has been found that the transition-state energy of simple dehydrogenation reactions correlates with the final state energy of that reaction.[21] Transition-state scaling relations for the four different hydrogenation reaction steps are shown in Figure 3. There is a fairly good

relationship between the transition-state energy and the energy of the dehydrogenated state. Note that the correlation is between the transition state and the dehydrogenated state of the molecules. Since we are investigating hydrogenation of CO to methanol, the transition states are correlated with the initial state of the hydrogenation step of the corresponding intermediate. Both adsorbates of the initial step scale with ΔE_C and ΔE_O via the scaling relations described above. The transition state energies are hence described entirely by the carbon and oxygen chemisorption energies, ΔE_C and ΔE_O.

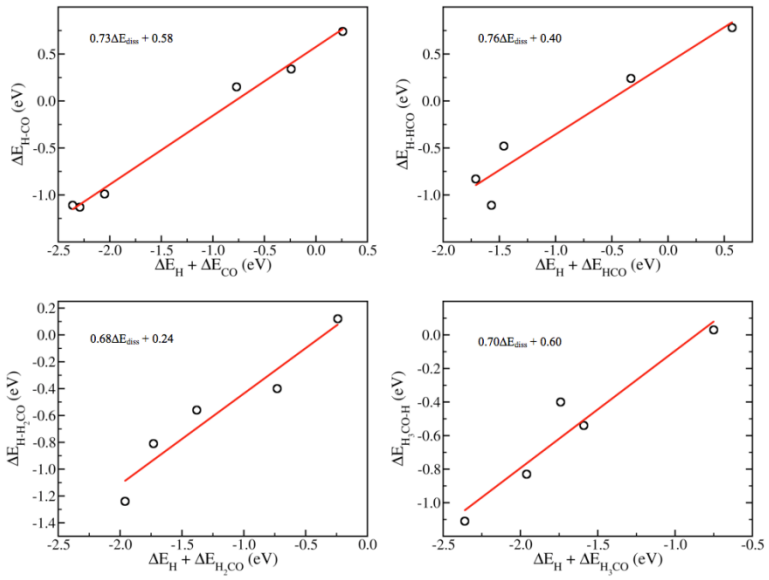

***Figure 3**. Scaling relations of transition state energies of the 4 different reaction steps of the lowest energy pathway from Figure 1. The transition state energies are calculated on the stepped (211) surfaces of various transition metals and are taken relative to CO and H_2 in the gas-phase. Zero-point corrections are not included. Energies are plotted as a function of the dissociated molecules, ΔE_{diss} (the initial states in the pathway from Figure 1). The red line is obtained by the best fit through data points; the slope and intercept of the fit is given in each figure.*

We will now describe the kinetics of methanol synthesis from CO and H_2. The following reaction steps are involved in the hydrogenation of CO:

(1) $CO + * \rightarrow CO*$
(2) $H_2 + 2* \rightarrow 2H*$
(3) $CO* + H* \rightarrow HCO* + *$ Rate determining step
(4) $HCO* + H* \rightarrow H_2CO* + *$
(5) $H_2CO* + H* \rightarrow H_3CO* + *$
(6) $H_3CO* + H* \rightarrow H_3COH + 2*$ Rate determining step

where * denotes an empty site on the catalytic surface. Inspection of the pathway on the Cu(211) surface reveals the first hydrogenation of CO to HCO as well as the last

hydrogenation of H_3CO to methanol are possible rate determining steps. In the vicinity of Cu in the (ΔE_C, ΔE_O) plane, we will assume this to hold generally.

In order to establish a relationship for the CO hydrogenation activity, a micro-kinetic model was developed which is based on the six elementary reaction steps (1-6). We solve these reaction rates analytically under the assumption that reactions (3) and (6) are rate determining, while all other reactions are in quasi-equilibrium. For the best catalysts coverages are found to be small and hence we do not include adsorbate-adsorbate interactions in this study. Another consequence is that the mean field model is adequate. The overall rate (turnover frequency) can be written as:

$$R_{tot} = R_3 = k_3 \Theta_{CO} \Theta_H \Theta_*^2 (1-\gamma_3)$$

with the rate constant, k_3:

$$k_3 = \frac{kT}{h} e^{\frac{-\Delta G^+}{kT}} = \frac{kT}{h} e^{\frac{-\Delta E^+}{kT}} e^{\frac{\Delta S^+}{k}}$$

and the six equilibrium constants, K_i :

$$K_i = e^{\frac{-\Delta G_i}{kT}} = e^{\frac{-\Delta E_i}{kT}} e^{\frac{\Delta S_i}{k}}$$

where i = 1-6. Both, ΔE^+ and ΔE_i are fully described by the two parameters, ΔE_C and ΔE_O as determined by the scaling relations for adsorbates and transition-states described above (see Figures 2 and 3). Zero-point energy and entropic contributions are calculated in the harmonic approximation. The fraction of free sites, Θ_*, and the approach to equilibrium (backward rate divided by forward rate) for reaction (3), γ_3, are obtained from the self-consistent steady-state solution to the micro-kinetic model. The total rate, R_{tot}, is hence fully described as a function of ΔE_C and ΔE_O.

Figure 4a shows the turnover frequency (TOF) as a function of the two descriptors, ΔE_C and ΔE_O, for a temperature of 523 K and a total pressure of 100 bar. The partial pressures of CO, H_2 and the product methanol are 45, 45, and 10 bar, respectively. Mapping of the TOF as a function of ΔE_C and ΔE_O gives a volcano shaped relation for methanol production. Cu is clearly identified as the only elemental transition metal close to the optimum. All other transition-metal catalysts are on the strong binding (Ni, Rh, Ru, Re, Fe, Pt, Pd) or weak-binding (Au, Ag) side of the reactivity volcano.

Figure 4b shows the selectivity between methanol and methane formation from synthesis gas. The selectivity is defined by the rate of methanol formation divided by

the sum of rates of methanol and methane formation. The methane volcano was described in ref [29] and similar reaction conditions have been used for the selectivity plot. Both Cu and Cu_3Zn are found to exhibit high selectivity towards methanol whereas metals like Ni, Ru, and Co have a high selectivity towards methane formation (Fig. 4b). This study does not include the formation of higher hydrocarbons and alcohols. Formation of these products need a more sophisticated kinetic analysis and will be subject of further studies.

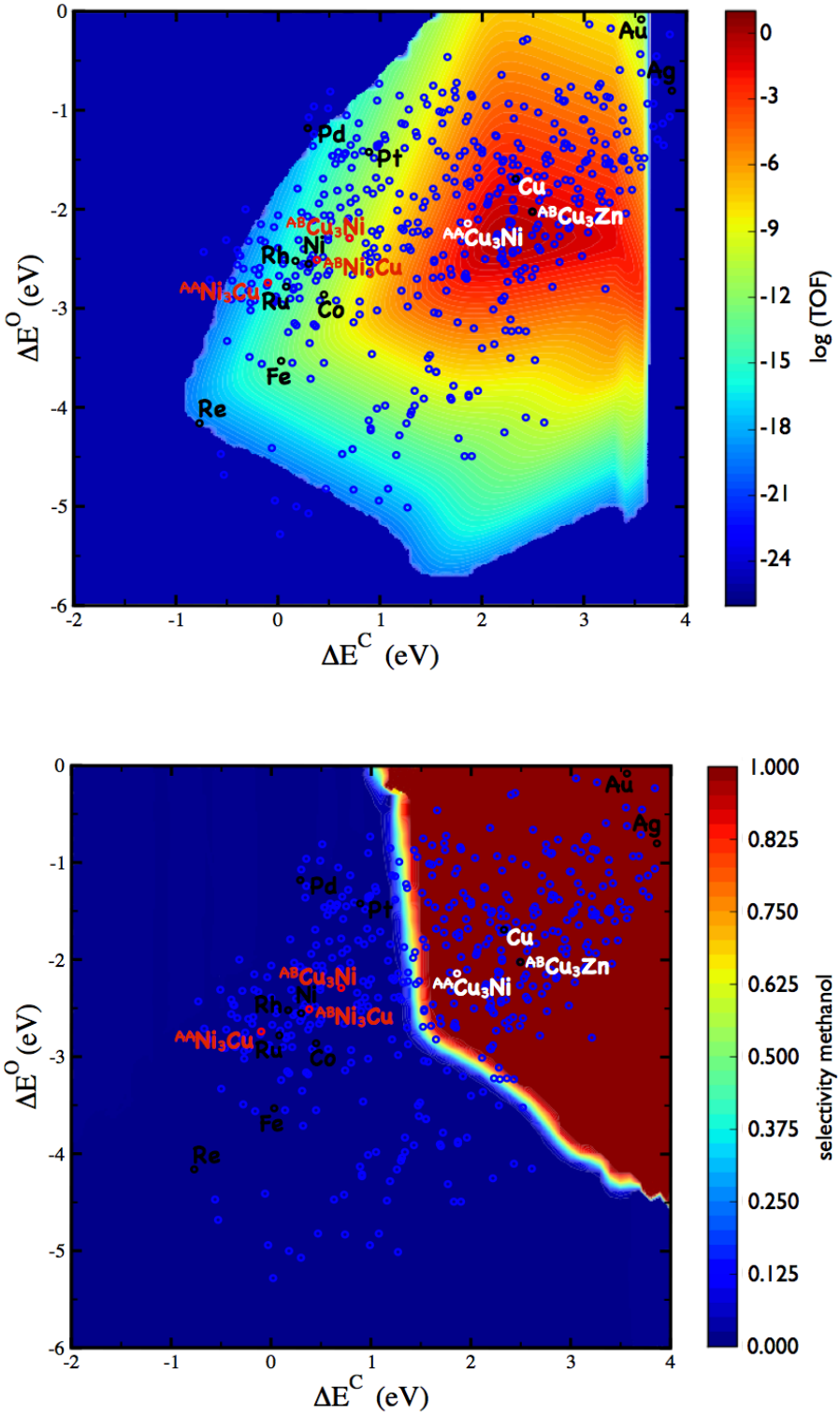

***Figure 4a**. Theoretical activity volcano for the production of methanol from CO and H_2. The turnover frequency is plotted as a function of carbon and oxygen binding energies. The carbon and oxygen binding energies for the stepped surfaces of selected transition metals are depicted. Small circles depict calculated carbon and oxygen binding energies for a range of binary alloys.*

Two different steps for either of Cu_3Ni and $CuNi_3$ alloys are depicted in red; the Cu step of Cu_3Ni is depicted in white. Cu and the AB step of Cu_3Zn are depicted in black. For the nomenclature of the steps see Figure 6. Reaction conditions are 523 K, 45 bar H_2, 45 bar CO, and 10 bar methanol. ***b****. Selectivity between methane and methanol formation as function of carbon and oxygen binding energies. The selectivity is defined as the rate towards methanol divided by the total rate of methanol and methane formation. Methane formation is calculated via a similar micro-kinetic model as given in ref [29] but with slightly different reaction conditions (523 K, 45 bar H_2, 45 bar CO, 5 bar CH_4, and 5 bar H_2O). Labels as in figure 4a.*

In order to identify candidate materials for methanol production, we screened a large number of bimetallic alloys with respect to their stability and activity. The bimetallic alloys were of the A_3B L_12 type and the AB BCC-B_2 type structures. We have calculated the stability of more than 1500 A_3B L_12 and more than 700 AB BCC-B_2 type alloys. Stable alloys (heat of formation negative) have been considered for further screening with respect to ΔE_C and ΔE_O. There are two different steps for the (211) surface of an A_3B L_12 structure, an AB and an AA step (see Figure 5, left), both of which have been included in this study. The corresponding steps of the AB BCC-B_2 structures also have two different step sites: AA and BB (see Figure 5, right). Both types of steps have been considered in the screening procedure. There are a number of different sites on the steps where adsorption of carbon and oxygen can take place. All different adsorption geometries have been calculated, the strongest binding site for each of the surfaces of each alloy is depicted in figure 4 (blue spheres circles).

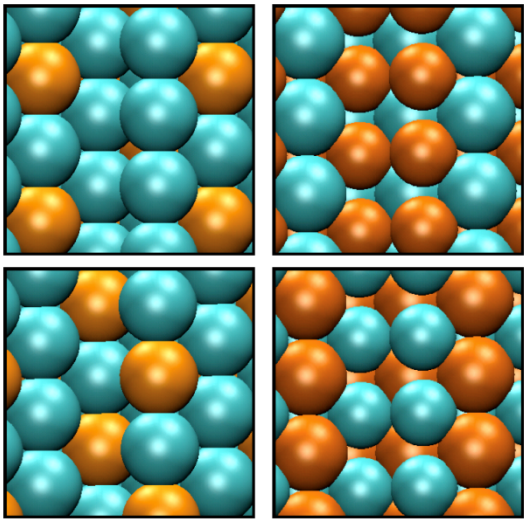

Figure 5*. Top left: structure of the 211 step of A_3B alloys (AA step). Bottom left: structure of the 211 step of A_3B alloys (AB step). Top right: structure of the step of AB alloys (AA step). Bottom right: structure of the step of AB alloys (BB step).* *Make another figure with side view*

While Cu is found to be the transition metal that is closest to the top of the volcano, there are several bimetallic alloys that are within the same region. Industrially, ZnO promotes Cu and we find that alloying of Zn into the Cu step increases its oxygen binding energy and moves Cu closer to the top of the volcano. An interesting alloy found in the screening procedure is Cu_3Ni. The pure Cu step (AA step) of Cu_3Ni is

calculated to have a more negative C and O chemisorption energy (stronger bonding) than Cu. Inspection of Figure 4 shows that the activity for the AA step of Cu_3Ni is predicted to be approximately that of pure Cu. Interestingly, the AA step of Cu_3Ni lies within the range for very selective methanol catalysts. The other step and both steps of Ni_3Cu on the other hand are calculated to produce mainly methane. The surface composition of CuNi alloys is hence very sensitive towards the selectivity of different products.

There are several reports on CuNi catalysts for synthesis gas conversion in the literature. Most catalysts produce a mixture of methanol, methane, hydrocarbons and higher alcohols.[37,38] Activity in methane production is not surprising since both the AB step (CuNi step) of $CuNi_3$ and the AA and AB steps of Ni_3Cu are calculated to have ΔE_C and ΔE_O that are within the region exhibiting high selectivity towards methane. The composition of the active site (the step) rather than the bulk composition of the bimetallic alloy will hence determine both the activity and selectivity of CuNi alloys. It has been shown experimentally that for certain preparation methods methanol selectivities up to 92% could be achieved.[39]

To test our theoretical predictions we have synthesized and characterized particles with different CuNi compositions and studied their methanol activity. Figure 6 shows the in-situ XRD patterns of a reduced $CuNi/SiO_2$ catalyst, which has been cooled down to room temperature after reduction in hydrogen at 300 °C. The XRD pattern shows only reflections of Cu and CuNi alloys. The ratio of Cu to Ni in the alloys is $Cu_{11}Ni_{14}$ when calculated according to Vegard's law.[40] The particle sizes are 47 and 14 nm for Cu and the $Cu_{11}Ni_{14}$ alloy, respectively, calculated by means of the Scherrer equation. In general, Cu and Ni can form a solid solution,[41] however, a separate Cu phase was also formed. This is probably due to the confinement effect of support pores. Cu sinters easily under strongly reducing conditions forming rather large particles (47 nm).

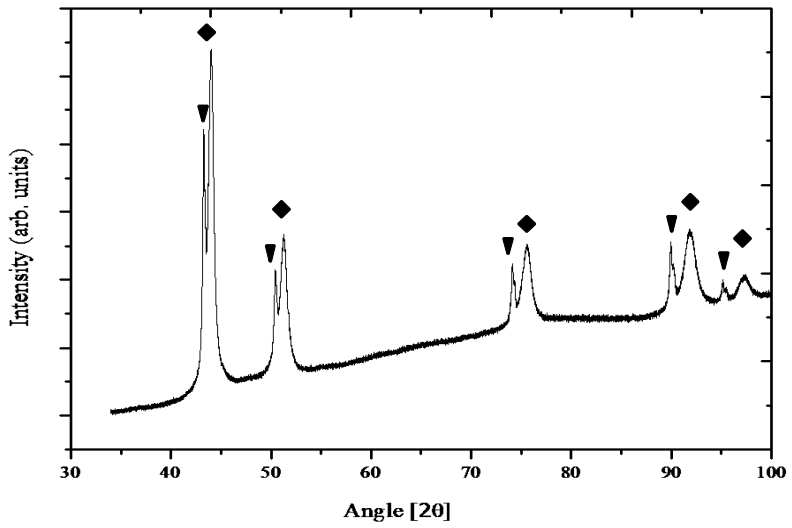

Figure 6. The XRD pattern of reduced $CuNi/SiO_2$ catalyst (cooled down to room temperature after reduction in hydrogen at 300 °C); ▼ - metallic Cu, ◆ - CuNi alloy.

The reduced $Cu/ZnO/Al_2O_3$ catalyst shows distinguished Cu and ZnO peaks with the average particle size of metallic Cu being about 6 nm, and about 3 nm for ZnO.

The ICP-OES elemental analysis results for $CuNi/SiO_2$ and $Cu/ZnO/Al_2O_3$ catalysts are listed in Table 1. For $CuNi/SiO_2$ sample, the original sample was designed as 20 wt% CuNi loading on SiO_2, whereas the measured loading was 17.6%. The deviation may be caused by loss of Cu and Ni salts during the preparation procedure. The Cu/Ni and Cu/Zn atomic ratio were close to the expected ratio.

Table 1. *Elemental analysis results of $CuNi/SiO_2$ and $Cu/ZnO/Al_2O_3$ samples*.

Catalysts	*Analyzed Loading (wt%)*		*Cu/Ni or Cu/Zn (atomic ratio)*	
	Cu	*Ni or Zn*	*nominal*	*measured*
$CuNi/SiO_2$	9.2	8.4	1.00	1.02
$CuZnO/Al_2O_3$	44.7	22.0	2.00	2.09

Table 2 shows the estimated particle diameters obtained for $CuNi/SiO_2$ and $Cu/ZnO/Al_2O_3$ samples as measured by TEM and XRD. The samples have been reduced in-situ. The weight of the active materials and the active surface area is also shown in Table 2

Table 2. *Estimated particle diameters, weight fraction of the active material and the active surface area of $CuNi/SiO_2$ and $Cu/ZnO/Al_2O_3$ samples*.

Sample	$d_{p,XRD}$ [a)] [nm]	$d_{p,TEM}$ [b)] [nm]	$m_{active\ materials}$ [c)] [g/g_{cat}]	ASA [d)] [m^2/g]
$CuNi/SiO_2$	14	7.8	0.176	8.38
$CuZnO/Al_2O_3$	6	-	0.714	79.3

[a)] Average crystal size as determined from peak broadening according to the Scherrer equation. [b)] Average particle size as determined by in-situ TEM. [c)] Weight of active material (metallic Cu and Ni for $CuNi/SiO_2$, Cu and ZnO for $Cu/ZnO/Al_2O_3$) per gram of catalyst precursor, which is calculated according to ICP-OAS. [d)] Active surface areas (ASA) of catalysts calculated from the particle sizes as determined by in-situ XRD.

The activity and selectivity of $CuNi/SiO_2$ and $Cu/ZnO/Al_2O_3$ catalysts for CO hydrogenation at various conditions are shown in Table 3. The main product that was observed for the $CuNi/SiO_2$ catalyst was methanol at all tested reaction conditions. Trace amounts of C_{2+} oxygenates (including dimethyl ether (DME) and ethanol) and hydrocarbons (HC) (including methane and ethane) have also been detected. The activity increases with an increase of reaction temperature (250 to 300 °C) while the selectivity towards methanol remains almost constant (99.2 and 99 mol%).

Table 3. *Behavior of $CuNi/SiO_2$ and $Cu/ZnO/Al_2O_3$ catalysts in CO hydrogenation at steady state at 100 bar, and H_2/CO = 1.0 vol/vol.*

Catalysts	T [ºC]	GHSV [h^{-1}]	X_{CO} [mol%]	Carbon based, CO_2-free selectivity [mol%]			$MeOH_{STY}$	TOF[a)]
				MeOH	C_{2+} oxygenates	HC	$g/(kg_{cat}·h)$	$mol_{MeOH}m^{-2}s^{-1}$
$CuNi/SiO_2$	250	2000	5.2	99.2	0.4	0.4	65	$6.7·10^{-5}$
$CuNi/SiO_2$	275	2000	12.1	99	0.4	0.6	167	$1.7·10^{-4}$
$CuNi/SiO_2$	300	4160	11.2	99	0.5	0.5	330	$3.4·10^{-4}$
$Cu/ZnO/Al_2O_3$	250	16000	7.2	99	0.9	0.1	842	$9.2·10^{-5}$
$Cu/ZnO/Al_2O_3$	275	16000	13.5	97.6	2.1	0.3	1315	$1.4·10^{-4}$
$Cu/ZnO/Al_2O_3$	300	32000	12.7	96.3	2.8	0.9	2666	$2.9·10^{-4}$

[a)] Molar amount of methanol based on active surface area of catalysts.

The *in-situ* XRD patterns show that the reduced $CuNi/SiO_2$ sample is composed of two phases, Cu particles and the CuNi alloy. There was no trace of elemental Ni that would exhibit methanation activity.[42] The major part of the reduced $CuNi/SiO_2$ catalyst is composed of the CuNi alloy (about 88 mol % according to the alloy molar ratio of Cu:Ni = 11:14, which was synthesized in a molar ratio of 1:1, and 1.02:1 determined by ICP-OAS). It is hence reasonable to assume that the main active phase for methanol synthesis is CuNi. Comparably, $Cu/ZnO/Al_2O_3$ exhibits fairly high activity towards methanol synthesis, it is, however, slightly less selective at higher temperatures.

In order to get a better estimate of the activity of the surface of $CuNi/SiO_2$ in comparison to $Cu/ZnO/Al_2O_3$ the turnover frequency (TOF) based on the active surface area was used instead of the space time yield (STY). As can be seen from Table 3, the TOF of $CuNi/SiO_2$ is within the same order of magnitude as calculated for $Cu/ZnO/Al_2O_3$. While being slightly less active at 250 °C, conversion is slightly higher at 275 and 300 °C. Even though the TOF can be seen as a rough estimate only, it should be mentioned that it agrees reasonably well with the position of $^{AA}Cu_3Ni$ relative to Cu in the methanol volcano (see Figure 4a).

Figure 7 shows the CO conversion and the CO_2-free alcohol selectivity as a function of time on stream for both, $CuNi/SiO_2$ and $Cu/ZnO/Al_2O_3$. For $CuNi/SiO_2$, CO conversion increases from 2.4 to 5.2 mol% while the selectivity to methanol increases from 95 to 99.2 mol% within the first 16 h after which the performance stabilizes. A similar tendency was observed at 275 °C where the CO conversion increased from 9.3 to 12.2 mol% within 12 h.

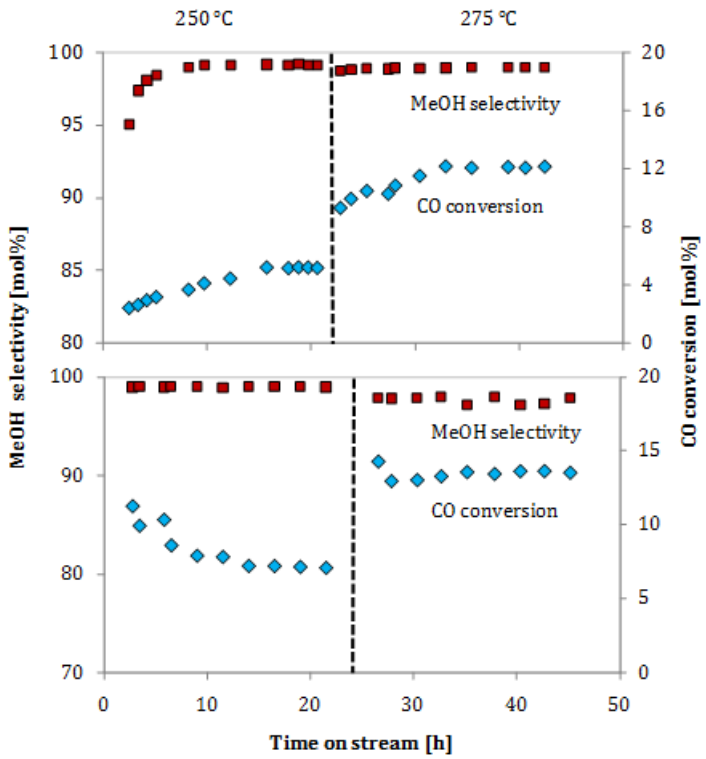

Figure 7 (top). CO conversion (blue diamonds) and methanol selectivity (red squares) as a function of the time on stream for the CuNi/SiO_2 catalyst. Reaction conditions are: P = 100 bar, T = 250 and 275 °C, GHSV = 2000 h^{-1}, Feed: H_2/CO =1 (vol/vol). ***(bottom)*** CO conversion (blue diamonds) and methanol selectivity (red squares) as a function of the time on stream for the Cu/ZnO/Al_2O_3 catalyst. Reaction conditions are: P = 100 bar, T = 250 and 275 °C, GHSV = 16000 h^{-1}, Feed: H_2/CO =1 (vol/vol).

The conversion and selectivity of the Cu/ZnO/Al_2O_3 catalyst as a function of time on stream is shown in Figure 7 (bottom). The CO conversion decreased from 11.3 to 7.2 mol% within the first 14 h of testing. This deactivation phenomenon is a typical problem for commercial methanol synthesis catalysts.[6,7] The predominant path of deactivation is related to the sintering of the copper particles reducing the active surface area. Another deactivation pathway of the Cu/ZnO/Al_2O_3 catalyst is due to brass formation in the highly reducing CO/H_2 gas mixture in the absence of CO_2.[43]

Given the high selectivity that could be obtained with CuNi catalysts, the question arises as to how the step configuration of the Ni-Cu alloy is controlled, since the two elements mix readily at many different concentrations. To a first approximation one would expect Ni to segregate to the step site due its higher binding to CO. This should lead to an increase in methane production due to a shift in carbon and oxygen binding and hence a decrease in methanol selectivity over time. We observed, however, a remarkably high selectivity towards methanol even after 70 hours on stream. This indicates that the CuNi particles are mainly composed of the $^{AA}Cu_3Ni$ step, as this is the only surface composition of CuNi that is predicted to have high activity and selectivity towards methanol. The important question is why this step is stable, particularly at high pressures of CO.

In a related study, it has been shown recently that the less reactive component of CuPt near-surface alloys, Cu segregates to the surface at elevated pressures of CO.[44] Surface segregation of Cu was found to be driven by the formation of a CO/CuPt surface alloy where CO is binding on-top of a Pt atom that is surrounded by 6 Cu atoms. This formation can be explained by the fact that Pt that is surrounded by Cu has a substantially stronger Pt-CO bond as compared to a Pt overlayer due to higher energy d states.

We have investigated the CuNi system theoretically to help establishing the surface structure under reaction conditions that is at high pressures of CO. DFT calculations of a (√3 x √3)R30° unit cell with different concentrations of Cu and Ni in the first and second layer were used to identify the most stable surface. Due to its lower surface energy, Cu is most stable in the first layer of CuNi when there are no adsorbates present. In the presence of CO, however, Ni segregates to the surface due to its higher bond strength towards CO. Interestingly, the most stable structure in the presence of CO is composed of 1/3 ML of Ni and 2/3 ML of Cu where CO binds on-top of a Ni atom as illustrated in Figure 8. As shown in Table 3, the CO binding energy increases from -1.32 eV for a pure Ni overlayer to -1.92 and -1.52 for $NiCu_2$ overlayer structures. CO induced segregation energies are -0.77 and -0.63 eV for the $NiCu_2$ overlayer structures when compared to a pure Ni overlayer (see Table 4).

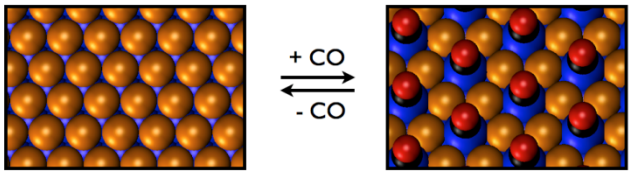

***Figure 8**. Illustration of CO induced surface segregation of a 1/3 ML Ni to the first layer of an fcc(111) surface composed of Cu and Ni. Left: Cu overlayer on CuNi alloy. Right: CO adsorbed on Ni surrounded by Cu. Blue atoms are Ni; orange atoms are Cu; black atoms are C; red atoms are oxygen.*

***Table 4.** Segregation energies for Cu in Ni with and without adsorbed CO on the 111 plane.[a]*

Cu content (ML)	Distribution in 1st and 2nd layer (1st:2nd)	ΔE_{seg} in vacuum[b]	ΔE_{CO}[c]	ΔE_{segCO}[d]
0	Ni	-	-1.32	-
1/3	Ni_2Cu_1:Ni_3Cu_0	-0.64	-1.37	-0.70
	Ni_3Cu_0:Ni_2Cu_1	-	-1.32	-
2/3	Ni_1Cu_2:Ni_3Cu_0	-0.16	-1.92	-0.77
	Ni_2Cu_1:Ni_2Cu_1	-0.24	-1.03	0.04
	Ni_3Cu_0:Ni_1Cu_2	-	-1.31	-
1	Ni_0Cu_3:Ni_3Cu_0	-0.80	-0.41	0.08
	Ni_1Cu_2:Ni_2Cu_1	-0.40	-1.52	-0.63
	Ni_2Cu_1:Ni_1Cu_2	-0.16	-1.35	-0.22
	Ni_3Cu_0:Ni_0Cu_3	-	-1.29	-

[a] Segregation energies are for a (√3 x √3)R30° four layer slab of Ni where the first two rows are composed according to column 2. All energies are in eV. [b] Segregation energies relative to the state where all Cu atoms are present in the second layer. [c] CO adsorption energies for 1/3 ML of CO. [d] CO induced segregation energy compared to the state where all Cu atoms are present in the second layer.

Having established the composition of the (111) surface of a CuNi alloy, we will now investigate the stepped (211) surface of Cu_3Ni in order to identify the composition of the active site. The (211) plane of the Cu_3Ni alloy can be cut to produce two different step sites, an AA step that is composed of Cu atoms and an AB step where Cu and Ni atoms alternate (see Figure 5). We calculated both, the CuCu and CuNi step with and without CO adsorbed (see Table 5).

Table 5. *Segregation energies for the CuCu and CuNi step of Cu_3Ni with and without adsorbed CO.* [a]

	CuCu step			CuNi step		
	Clean	Ni row	Cu row	Clean	Ni row	Cu row
ΔE_{seg}	-	1.10	-0.07	-	0.54	-0.42
ΔE_{CO}	-1.59	-2.07	-0.71	-1.80	-2.05	-1.63
ΔE_{segCO}	-1.59	-0.96	-0.77	-1.80	-1.51	-2.06

[a] *Segregation energies are for a (211) four layer slab of Cu_3Ni. Energies are for the clean steps, steps with an additional row of Ni atoms and steps with an additional row of Cu atoms. Segregation energies (ΔE_{seg}) are relative to Ni (Cu) in the bulk. CO adsorption energies* (ΔE_{CO}) *are calculated relative to CO in the gas-phase. CO induced segregation energies* (ΔE_{segCO}) *are calculated relative to the Ni (Cu) in the bulk and CO in the gas-phase. All energies are in eV.*

CO adsorbs on the Ni atoms behind the CuCu step with -1.59 eV. Adsorption on top of Ni of the CuNi step is larger being -1.80 eV. Segregation of Ni to the CuCu step costs 1.10 eV (per two Ni) when compared to bulk Ni. CO adsorbs with -2.07 eV in the bridge position between two Ni atoms. CO induced segregation, however, amounts only to -0.96 eV since segregation of Ni is uphill in energy. Importantly, this value is smaller than CO adsorption on Ni behind the CuCu step and thus prevents segregation of Ni to the step.

Segregation of Ni to the CuNi step is slightly less costly (0.54 eV per two Ni) and yields approximately the same CO adsorption energy (-2.05 eV) as found for Ni segregated to the CuCu step (the CO sits threefold between the two Ni along the step and one Ni behind the step). CO induced Ni segregation is hence -1.51 eV, being less than CO adsorption on the clean CuNi step. Importantly, Cu segregation to the step is downhill by -0.42 eV (per two Cu atoms). CO adsorption on the Ni atom that now is located behind these Cu atoms is -1.63 eV, similar to the value calculated for CO adsorption ontop Ni behind the CuCu step. CO induced segregation of Cu to the CuNi step amounts hence -2.06 eV, which is more than CO adsorption on the CuNi step. The active site of CuNi will hence have Cu along the step under methanol synthesis reaction conditions (high CO pressure). A picture of the active site is displayed in Figure 9. Importantly, CO adsorbed on Ni is basically a spectator molecule determining the surface structure while methanol synthesis is taking place on the Cu steps.

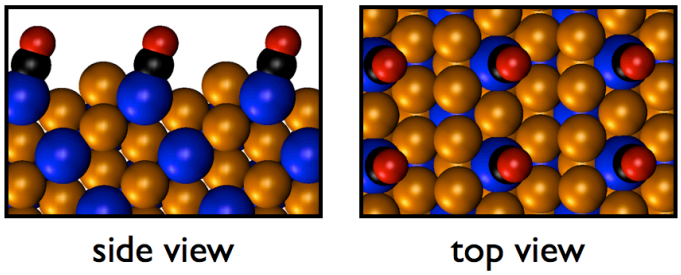

***Figure 9**. The active site of the Cu_3Ni catalyst under methanol reaction conditions (high CO pressure). CO hydrogenation occurs at the step of the site of the alloy, which is composed out of Cu atoms. CO strongly adsorbed on Ni holds the Cu step in place. Blue atoms are Ni; orange atoms are Cu; black atoms are C; red atoms are oxygen.*

Conclusion

We investigated methanol synthesis from CO and H_2 over transition metal surfaces. Methanol formation was found to proceed via hydrogenation of the carbon end of CO to methoxy, which in turn is hydrogenated to methanol. Hydrogenation of CO and methoxy are the most difficult steps with the highest barriers. We extended the study to other transition metal surfaces and found that all intermediates involved in the reaction scale with the adsorption energy of carbon or oxygen or a combination of both of them. In most cases the scaling was found to follow simple bond counting arguments.[15,28] Similarly, the transition state energies were found to scale with the dissociated state (BEP relation) and hence with ΔE_C and ΔE_O as well.

We developed an analytical micro kinetic model that assumes hydrogenation of CO and methoxy as being rate determining and constructed a volcano-shaped relationship for methanol synthesis that is based on scaling relations and hence maps out the activity towards methanol as a function of ΔE_C and ΔE_O. A comparison with the rates for methane formation[29] gives a selectivity map between methane and methanol. We screened a number of binary alloys as leads for methanol synthesis candidates and identified CuNi alloys as being interesting. In particular, the $^{AA}Cu_3Ni$ step was predicted to exhibit high activity and selectivity towards methanol.

We synthesized the calculated candidates, CuNi alloy catalysts, and a model commercial $Cu/ZnO/Al_2O_3$ catalyst and tested them in a fixed-bed continuous-flow reactor for CO hydrogenation. The turnover frequency for a $CuNi/SiO_2$ catalyst indeed was at the same level as the $Cu/ZnO/Al_2O_3$ model catalyst. It even has a slightly higher selectivity to methanol than the model methanol synthesis catalyst in a pure CO/H_2 atmosphere. The high activity and selectivity of silica supported CuNi alloy catalyst agreed with the fact that the DFT calculations identified CuNi alloy ($^{AA}Cu_3Ni_1$) catalyst as highly active and selective catalysts for the hydrogenation of CO to form methanol. Additionally, no deactivation took place, but instead an activation process was observed during a total 73 h test of time on stream for the CuNi alloy catalyst.

However, long term testing should be carried out as well as optimization of that catalyst composition and preparation procedure.

DFT calculations of CuNi surface structures identified Cu_2Ni as being stable at elevated pressures of CO. Importantly, the step of Cu_3Ni was predicted to be composed of Cu atoms while CO binds to Ni that sits behind the step. This unusual surface structure is believed to be the reason for the high selectivity and also the long-term stability of CuNi catalysts.

In summary, CuNi alloys show some promising first results for the development of durable methanol synthesis catalysts. More studies, however, need to be conducted in the future in order to identify catalysts that would be able to improve or replace commercial $Cu/ZnO/Al_2O_3$ catalysts. In addition, this study needs to be extended to include CO_2 as a possible feed, which calls for the inclusion of the water-gas-shift reaction into the micro kinetic model.

Experimental Details

Density Functional Theory Calculations

Density functional theory calculations were carried out using the Dacapo code,[45] which uses a plane wave implementation to describe the valence electrons and Vanderbilt ultrasoft pseudopotentials[46] to represent the ionic cores. The kinetic energy cutoff was 340 eV with a density cutoff of 500 eV. All calculations were performed using the RPBE [47] functional, which uses a generalized gradient approximation. The self-consistent electron density was determined by iterative diagonalization of the Kohn-Sham Hamiltonian, with the occupation of the Kohn-Sham states being smeared according to a Fermi-Dirac distribution with a smearing factor of k_bT = 0.1 eV and Pulay mixing of the resulting electron densities.[48] Spin-polarized calculations have been performed for Fe, Co and Ni.

The stepped surface structures were modeled by 9 layer slabs with (1x3) unit cells. The uppermost close-packed surface layer together with the adsorbates was allowed to relax, whereas the remaining layers have been kept fixed in their RPBE calculated bulk positions. In all cases a sampling of 3x3x1 special k-points of the Monkhorst-Pack type was used to model the 1st Brillouin zone.[49] Increasing the number of *k*-points has shown a negligible effect on adsorption energies. The periodic slab approximation was used and stepped surfaces have been modeled by fcc(211) for (100) symmetry steps and fcc(331) for (111) symmetry steps. The slabs were separated by at least 12 Å of vacuum. Lattice constants of binary alloys were calculated in a periodic cell consisting of 4 atoms with a 8x8x8 *k* point sampling. Slabs of binary alloys were modeled as described above for transition-metal surfaces.
Transition state energies were determined using a fixed bond-length approach in which the distance between the involved atoms is increased until a saddle-point was

reached. The vibrational frequencies that were used to determine the zero-point energy and entropy corrections were calculated in the harmonic normal-mode approximation.

Catalyst preparation

Silica supported CuNi catalyst (20 wt % Cu+Ni loading on silica, molar ratio of Cu:Ni = 1:1) oxide precursors were prepared by the incipient wetness impregnation method. First, an aqueous solution was prepared by dissolving $Cu(NO_3)_2 \cdot 3H_2O$ and $Ni(NO_3)_2 \cdot 6H_2O$ in de-ionized water. Then SiO_2 (with a BET specific surface area of 250 m^2/g) pellets was impregnated by the aqueous solution. After 1 h aging, catalysts were dried at 100 °C in air, and subsequently calcined at 400 °C in air for 4 h with a heating rate of 1.5 °C/min.

A model methanol synthesis $Cu/ZnO/Al_2O_3$ catalyst was prepared by a coprecipitation method similar to that used by Baltes et al.[50] An aqueous solution of metal nitrates [($Cu(NO_3)_2$ (0.6 mol/L), $Zn(NO_3)_2$ (0.3 mol/L), $Al(NO_3)_3$ (0.1 mol/L))] was coprecipitated by a solution of Na_2CO_3 (1 mol/L) . During the precipitation process, pH was maintained at 7±0.1, temperature was kept at 60 °C, and then aged at 60 °C for 1 h. Afterwards the precipitate was filtered and washed three times with demineralized water followed by drying overnight at 80 °C and calcining at 300 °C under air for 3 h (heating rate 2 °C /min).

All chemicals were supplied by Sigma-Aldrich except SiO_2 that was offered by Saint-Gobain Norpro. All the catalyst precursors have been pressed, crushed and sieved to a size range of 0.6-1.4 mm.

Catalyst characterization

The chemical composition of $CuNi/SiO_2$ and $Cu/ZnO/Al_2O_3$ catalysts were determined by an inductively coupled plasma-optical emission spectrometer (ICP-OES, Perkin–Elmer, model Optima 7300) and using Ar as plasmogene.

In-situ XRD was applied with a PANalytical X'Pert PRO diffractometer equipped with an Anton Paar XRK 900 *in-situ* cell (APC), a gas flow control system, a Ni filter and a slit for H_2-TPR. $CuNi/SiO_2$ and $CuZnO/Al_2O_3$ precursors were heated in flowing 20 mol% H_2/He up to 300 °C and 220 °C, respectively. The average particle diameter ($d_{p,XRD}$) of reduced phases (cooling down to room temperature after reduction) were determined by means of the Scherrer equation [reference?].

In situ TEM was performed using an FEI Titan 80-300kV TEM equipped with an environmental cell and a differential pumping system.[51,52] This microscope permits the acquisition of TEM images of samples during the exposure to reactive gases (up

to ca. 15 mbar) and elevated temperatures. For the present experiments, the specimen was imaged during the exposure to 1.3 mbar H_2. The specimen was heated in the gas environment at a rate of 7 °C/min from room temperature up to 300 °C for $CuNi/SiO_2$ and 220 °C for $Cu/ZnO/Al_2O_3$ catalyst precursors. The TEM imaging was performed after drift-stabilization of the sample holder.

Catalyst Activity Testing

The performance of catalysts for CO hydrogenation was evaluated in a fixed-bed continuous-flow reactor (detailed descriptions of the experimental setup and the experimental procedure have been provided elsewhere)[53,54,55] with an online GC-FID/TCD detection system (6890N from Agilent Technologies). A bubble flow meter was used for determination of volumetric flow rate of the reactor effluent. Prior to the reaction, all catalysts oxide precursors were pre-reduced in situ by a 20 vol% H_2/N_2 mixture for $CuNi/SiO_2$ at 300 °C and 1.4 vol% H_2/N_2 at 220 °C $Cu/ZnO/Al_2O_3$ for 12-14 h, with a heating rate of 1 °C/min. The conversion of CO (X_{CO}) is calculated from the molar flow rates of CO into and out of the reactor:

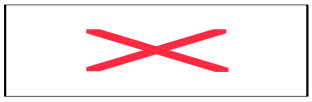

The conversion of CO_2 (X_{CO2}) is calculated from the molar flow rates of CO_2 into and out of the reactor:

$$X_{CO_2} = \frac{F_{CO_2}^{in} - F_{CO_2}^{out}}{F_{CO_2}^{in}} \cdot 100\%$$

The CO_2-free selectivity to product is based on the total number of carbon atoms except CO_2 in the products:

$$S_i = (n_i M_i) / (\sum n_i M_i) \cdot 100\%$$

Where n_i ($n_i \geq 1$) is the number of carbon atoms in the product i, M_i is the detected percentage of product i in the gas.

The mass balances for carbon generally fulfilled to within 5 mol%.

Acknowledgement

F.S., F.A.-P., and J.K.N. wish to acknowledge support from the (U.S.) Department of Energy (DOE), Office of Basic Energy Sciences.

The experimental work is financed by the Technical University of Denmark, Haldor Topsøe A/S, and the Danish Ministry for Science, Technology and Development under the "Catalysis for Sustainable Energy" initiative. We thank Mr. Helge Kildahl Rasmussen from DTU Physics for aid in the XRD measurement, and Mr. Irek

Sharafutdinov for help with preparation of the model methanol synthesis catalyst and ANKA for providing beamtime at ANKA-XAS as well as EU for financial support of the synchrotron radiation experiments

References

[1] J.B. Hansen, P.E.H. Nielsen, in: G. Ertl, H. Knözinger, F. Schüth, J. Weitkamp (Eds.), Handbook of Heterogeneous Catalysis, Wiley VCH, 2008, p. 2920.
[2] G.A. Olah, Angew. Chem. Int. Ed. 44 (2005) 2636.
[3] S. Lee, in: Methanol Synthesis Technology, CRC Press, 1989.
[4] M. Behrens, F. Studt, I. Kasatkin, S. Kühl, M. Hävecker, F. Abild-Pedersen, S. Zander, F. Girgsdies, P. Kurr, B. Kniep, M. Tovar, R.W. Fischer, J.K. Nørskov, R. Schlögl, submitted.
[5] J.-D. Grunwaldt, A.M. Molenbroek, N.-Y. Topsøe, H. Topsøe, B.S. Clausen, J. Catal. 194, (2000) 452.
[6] J.C.J. Bart, R.P.A. Sneeden, Catal. Today 2 (1987) 1.
[7] J.B. Hansen, AlChE Spring National Meeting, Orlando, Fl, 1990.
[8] H.Y. Chen, J. Lin, K.L. Tan, J. Li, Appl. Surf. Sci. 126 (1998) 323.
[9] J. Li, W. Zhang, L. Gao, L. Gu, K. Sha, H. Wan, Appl. Catal. A 165 (1997) 411.
[10] R.A. Köppel, C. Stöcker, A. Baiker, J. Catal. 179 (1998) 515.
[11] T. Fujitani, M. Saito, Y. Kanai, M. Takeuchi, K. Moriya, T. Watanabe, M. Kawai, Y. Kakumoto, Chem. Lett. (1993) 1079.
[12] M. Saito, J.G. Wu, H. Mabuse, Catal. Lett. 68 (2000) 55.
[13] P.J. Berlowitz, D.W. Goodman, J. Catal. 108 (1987) 364.
[14] X. Youchang, B. M. Naasz, G. A. Somorjai, Appl. Catal. 27 (1986) 233.
[15] F. Abild-Pedersen, J. Greeley, F. Studt, J. Rossmeisl, T.R. Munter, P.G. Moses, E. Skúlason, T. Bligaard, J. K. Nørskov, Phys. Rev. Lett. 99 (2007) 016105.
[16] V. Pallassana, M. Neurock, J. Catal. 191 (2000) 301.
[17] J.K. Nørskov, T. Bligaard, A. Logadottir, S. Bahn, L.B. Hansen, M. Bollinger, H. Bengaard, B. Hammer, Z. Sljivancanin, M. Mavrikakis, Y. Xu, S. Dahl, C.J.H. Jacobsen, J. Catal. 209 (2002) 275
[18] A. Michaelides, Z.P. Liu, C.J. Zhang, A. Alavi, D.A. King, P. Hu, J. Am. Chem. Soc. 125 (2003) 3704.
[19] T. Bligaard, J.K. Nørskov, S. Dahl, J. Matthiesen, C.H. Christensen, J. Sehested, J. Catal. 224 (2004) 206.
[20] S. Wang, B. Temel, J. Shen, G. Jones, L.C. Grabow, F. Studt, T. Bligaard, F. Abild-Pedersen, C.H. Christensen, J.K. Nørskov, Catal. Lett. 141 (2011) 370.
[21] S. Wang, V. Petzold, V. Tripkovic, J. Kleis, J. G. Howalt, E. Skúlason, E. M. Fernández, B. Hvolbæk, G. Jones, A. Toftelund, H. Falsig, M. Björketun, F. Studt, F. Abild-Pedersen, J. Rossmeisl, J.K. Nørskov, T. Bligaard, Phys. Chem. Chem. Phys. 13 (2011) 20760.
[22] L.C. Grabow, M. Mavrikakis, ACS Catal. 1 (2011) 365.
[23] Z.M. Hu, K. Takahashi, H. Nakatsuji, Surf. Sci. 442 (1999) 90.
[24] Y. Yang, J. Evans, J.A. Rodriguez, M.G. White, P. Liu, Phys. Chem. Chem. Phys. 12 (2010) 9909.

[25] I. Kasatkin, P. Kurr, B. Kniep, A. Trunschke, R. Schlögl, Angew. Chem. Int. Ed. 46 (2007) 7324.
[26] M.M. Günter, T. Ressler, B. Bems, C. Büscher, T. Genger, O. Hinrichsen, M. Muhler, R. Schlögl, Catal. Lett. 71 (2001) 37.
[27] W.J. Durand, A.A. Peterson, F. Studt, F. Abild-Pedersen, J.K. Nørskov, Surf. Sci. 605 (2011) 1354.
[28] E. Shustorovich, A.T. Bell, Surf. Sci. 205 (1988) 492.
[29] J.K. Nørskov, F. Abild-Pedersen, F. Studt, T. Bligaard, Proc. Natl. Acad. U.S.A. 108 (2011) 937.
[30] L.C. Grabow, F. Studt, F. Abild-Pedersen, V. Petzold, J. Kleis, T. Bligaard, J.K. Nørskov, Angew. Chem. Int. Ed. 50 (2011) 4601.
[31] G. Jones, J.G. Jakobsen, S.S. Shim, J. Kleis, M.P. Andersson, J. Rossmeisl, F. Abild-Pedersen, T. Bligaard, S. Helveg, B. Hinnemann, J.R. Rostrup-Nielsen, I. Chorkendorff, J. Sehested, J.K. Nørskov, J. Catal. 259 (2008) 147.
[32] H. Falsig, B. Hvolbæk, I.S. Kristensen, T. Jiang, T. Bligaard, C.H. Christensen, J.K. Nørskov, Angew. Chem. Int. Ed. 47 (2008) 4835.
[33] F. Studt, F. Abild-Pedersen, T. Bligaard, R.Z. Sørensen, C.H. Christensen, J.K. Nørskov, Science 320 (2008) 1320.
[34] M.P. Andersson, T. Bligaard, A. Kustov, K.E. Larsen, J. Greeley, Y. Johannessen, C.H. Christensen, J.K. Nørskov, J. Catal. 239 (2006) 501.
[35] J. Greeley, I.E.L. Stephens, A.S. Bondarenko, T.P. Johansson, H.A. Hansen, T.F. Jaramillo, J. Rossmeisl, I. Chorkendorff, J.K. Nørskov, Nature Chem. 1 (2009) 552.
[36] G. Jones, F. Studt, F. Abild-Pedersen, J.K. Nørskov, T. Bligaard, Chem. Eng. Sci. (2011), *66*, 6318.
[37] J. Llorca, R. de la Piscina, N. Homs, E.B. Pereira, P. Moral, G.A. Martin, Stud. Surf. Sci. Catal. 107 (1997) 9.
[38] S. Uchiyama, Y. Obayashi, M. Shibata, T. Uchiyama, N. Kawata, T. Konishi, J. Chem. Soc., Chem. Commun. (1985) 1071.
[39] E.B. Pereira, G.A. Martin, Appl. Catal. A: Gen. 103 (1998) 331.
[40] A.R. Denton, N.W. Ashcroft, Phys. Rev. A 43 (1991) 3161.
[41] H. Okamoto, Desk handbook: phase diagrams for binary alloys, Asm Intl, 2000.
[42] M. Araki, V. Ponec, J. Catal. 44 (1976) 439.
[43] T. van Herwijnen, W.A. de Jong, J. Catal. 34 (1974) 209.
[44] K.J. Andersson, F. Calle-Vallejo, J. Rossmeisl, I. Chorkendorff, J. Am. Chem. Soc. 131 (2009) 2404.
[45] The Dacapo plane wave / pseudopotential code is available as open source software at http://wiki.fysik.dtu.dk/dacapo.
[46] D. Vanderbilt, Phys. Rev. B 41 (1990) 7892.
[47] B. Hammer, L.B. Hansen, J.K. Nørskov, Phys. Rev. B 59 (1999) 7413.
[48] G. Kresse, J. Furthmüller, Comput. Mater. Sci. 6 (1996) 15.
[49] H.J. Monkhorst, J.D. Pack, Phys. Rev. B 13 (1976) 5188.
[50] C. Baltes, S. Vukojevic, F. Schüth, J. Catal. 258 (2008) 334.
[51] T.W. Hansen, J.B. Wagner, P.L. Hansen, S. Dahl, H. Topsøe, C.J.H. Jacobsen, Science 294 (2001) 1508.

[52] P.L. Hansen, J.B. Wagner, S. Helveg, J.R. Rostrup-Nielsen, B.S. Clausen, H. Topsøe, Science 295 (2002) 2053.
[53] J.M. Christensen, P.A. Jensen, A. Jensen, Ind. Eng. Chem. Res. 50 (2011) 7949.
[54] J.M. Christensen, P.A. Jensen, N.C. Schiødt, A.D. Jensen, ChemCatChem 2 (2010) 523.
[55] J.M. Christensen, P.M. Mortensen, R. Trane, P.A. Jensen, A.D. Jensen, Appl. Catal. A: Gen. 366 (2009) 29.